

論文 / 著書情報  
Article / Book Information

Title	Super Dragon: A 10-m-Long-Coupled Tendon-Driven Articulated Manipulator
Authors	Gen Endo, Atsushi Horigome, Atsushi Takata
Citation	IEEE Robotics and Automation Letters, Volume 4, Issue 2, pp. 934-941
Pub. date	2019, 5
Copyright	(c) 2019 IEEE. Personal use of this material is permitted. Permission from IEEE must be obtained for all other uses, in any current or future media, including reprinting/republishing this material for advertising or promotional purposes, creating new collective works, for resale or redistribution to servers or lists, or reuse of any copyrighted component of this work in other works.
DOI	<a href="https://dx.doi.org/10.1109/LRA.2019.2894855">https://dx.doi.org/10.1109/LRA.2019.2894855</a>
Note	This file is author (final) version.

# Super Dragon: A 10-m-long Coupled Tendon-driven Articulated Manipulator

Gen Endo<sup>1</sup>, Atsushi Horigome<sup>2</sup> and Atsushi Takata<sup>1</sup>

**Abstract**—The decommissioning of the Fukushima Daiichi Nuclear Power Plants is a national urgent problem in Japan. The distribution and characteristics of the fuel debris inside the nuclear reactor must be investigated to safely retrieve them. This study describes a 10 m-long articulated manipulator for investigation inside the primary container vessel. We employed a coupled tendon-driven mechanism and a gravity compensation mechanism using synthetic fiber ropes to design a lightweight and slender articulated manipulator. After discussing the basic principle and control algorithm, we focus on the detailed mechanical design of a prototype model. We confirmed its feasibility through basic motion experiments.

## I. INTRODUCTION

The decommissioning of the Fukushima Daiichi Nuclear Power Plants (NPPs) is a national urgent problem in Japan. More than 100 tons of nuclear fuel debris, which contains melted nuclear fuels and structural materials, is estimated to remain in each nuclear reactor. For the first time in July 2017, the International Research Institute of Nuclear Decommissioning (IRID) succeeded in obtaining visual images of the fuel debris in the Primary Container Vessel (PCV) in the No. 3 reactor by using a small-sized remotely operated underwater vehicle developed by Toshiba [2]. However, the captured images were partial and limited to the No. 3 reactor; thus, more investigations are still needed to fully understand the fuel debris distribution and characteristics.

A long-reach manipulator is required to investigate inside the PCV and retrieve the fuel debris in the future. IRID and Mitsubishi Heavy Industry developed a prototype model of a 6-degree of freedom (DoF) gigantic hydraulic manipulator (PA-2000) to retrieve fuel debris and internal structures [3]. The arm length and the weight were 7.1 m and 3500 kg, respectively. Although it can generate a large output force of 2000 kgf, it was not easy to deploy because of its large size and heavy weight.

The target task of this study is to investigate inside the PCV with a measurement device weighing 10 kg. The maximum reach is assumed to be 10 m considering the PCV size. The smaller access hole is more appropriate in preventing radiation leakage from the PCV. Thus, we try to minimize the arm diameter.

\*This work was supported by the New Energy and Industrial Technology Development Organization (NEDO)

<sup>1</sup>Gen Endo, and Atsushi Takata are with Department of Mechanical Engineering, School of Engineering, Tokyo Institute of Technology, 2-12-1 Ookayama, Meguro-ku, Tokyo, 152-8550, Japan [endo.g.aa@m.titech.ac.jp](mailto:endo.g.aa@m.titech.ac.jp)

<sup>2</sup>Atsushi Horigome is with the Department of Mechanical and Aerospace Engineering, Graduate School of Science and Engineering, Tokyo Institute of Technology

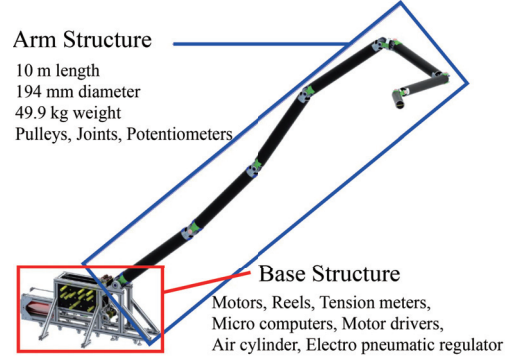


Fig. 1. Super Dragon: a 10 m-long coupled tendon-driven articulated manipulator (3DCAD model).

Some previous works about the long-reach articulated manipulator have been presented in the literature. To maintain an experimental tokamak nuclear fusion reactor (ITER), JET-EFDA developed a remote handling system with an 8 m-long horizontally extendable manipulator, called Octant 1 [4]-[6]. The Octant 1 had six segments serially connected by five yaw joints to mechanically support 100 kg payload at the end. All actuators were installed at the joints, and the estimated weight was approximately 7000 kg, which was very large.

The CEA LIST developed an 8.2 m-long multi-link manipulator with five modules of 160 mm diameter each [7]. The payload was 10 kg. Each module had both pitch and yaw joints, and the arm had a total of 10 DoF. Although each module included the gravity compensation mechanism for the pitch joint using a four-bar parallel linkage and a spring, the joint driving actuators were installed on each link. As a result, the weight of each module became 30 kg, and the total arm weight was 150 kg.

A 20 m-long balloon-type articulated manipulator was developed in our previous work [8]. It utilized thin pneumatic artificial muscles and helium gas buoyancy. The arm weight was only 1.2 kg, extremely easy for deployment, and essentially safe; however, its payload was limited only to 20 g.

We particularly focus herein on the coupled tendon-driven mechanism that can mount all actuators on the base structure. The mechanism permits us to design a lightweight arm structure while achieving a large payload at the end and a high radiation resistance. We have already confirmed the basic principle using a 2.4 m-long prototype [10]. The goal of this paper is to design and create a prototype of a 10 m-long tendon-driven articulated manipulator, called “Super Dragon” (Fig. 1), and confirm its feasibility through basic motion experiments.

## II. TARGET SPECIFICATION

We set our target specification for the long-reach articulated manipulator as follows based on the press releases from the Tokyo Electric Power Company (TEPCO), the information provided by IRID, and the hearings of the companies in charge of decommissioning:

- Length: 10 m
- Maximum arm diameter: 0.3 m
- Payload: 10 kg
- Total weight: 500 kg (arm: 100 kg; base: 400 kg)
- The total system can pass through an aperture of W 3.0 m  $\times$  H 2.5 m.

Fig. 2 shows the working image for deployment. An arm length of 10 m was determined by the PCV diameter of 20 m. The access hole diameter (X-6 penetration) was approximately 0.5 m; thus, we set the maximum arm diameter of 0.3 m considering the insertion motions by the articulated mechanism. We temporary assumed a 10 kg payload to deploy various measurement sensors, such as cameras, lighting, and radiation dose meter. The lighter and smaller arm permitted the ease of deployment of the robot in the NPPs; thus, we set a target total weight of 500 kg and a double-door size, which were extremely lightweight and compact compared to those in the previous works.

## III. MECHANISM

Coping with huge gravitational torques acting on the proximal joints is crucial when designing a long-reach cantilever manipulator. If we use a conventional precision reduction gear RV<sup>TM</sup> to support the gravity torque of 2450 Nm (assuming that the arm weight is 50 kg, and its center of mass is located in the middle of the arm), the weight of the reduction gear (RV-320C, Nabtesco) is 79.5 kg. This fact means that we cannot install the reduction gear mechanism on the joint like a conventional serial link manipulator.

In contrast, the coupled-tendon driven mechanism can share the gravitational torque by multiple wires, resulting in a lightweight and compact mechanism [10]. Moreover, we can achieve a higher load capacity with a slender mechanism if we introduce a thick rope to mainly support the gravitational torque depending on the global posture [14]. This section describes the outline of the basic principle of the coupled tendon driven mechanism with gravity compensation using a thick tendon.

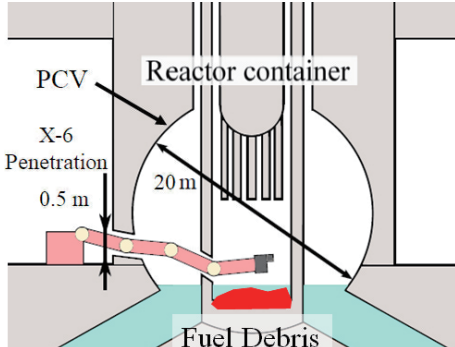


Fig. 2. Operating image of deployment in the Fukushima Daiich NPP.

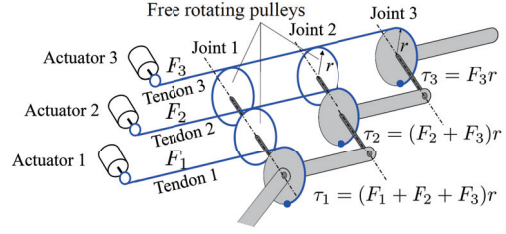


Fig. 3. Basic principle of the coupled tendon-driven mechanism.

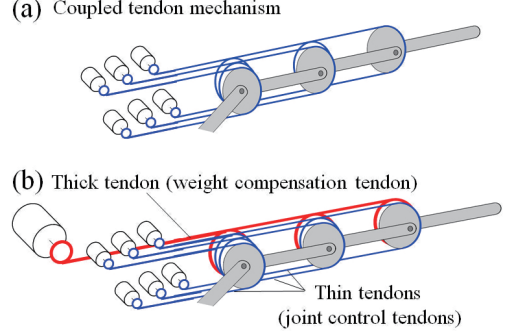


Fig. 4. Arrangement of tendons: (a) coupled tendon-driven mechanism and (b) weight compensation mechanism [18].

### A. COUPLED TENDON-DRIVEN MECHANISM

Figure 3 shows the basic principle of a coupled tendon-driven mechanism proposed in [9]. Each gray link is fixed to the gray pulleys with radius  $r = r_1 = r_2 = r_3$ , which freely rotates around the joint axis. The white pulleys with radius  $r$  are attached to the joint axis and also freely rotate around the joint axis. Tendon 3, which is fixed to the distal gray pulley to drive Joint 3, is wound around two proximal free pulleys and is pulled by the tension of  $F_3$ . Tendon 2, which is fixed to the second distal gray pulley to drive Joint 2, is wound around the proximal free pulley and is pulled by the tension of  $F_2$ . The tendon fixed to the proximal gray joint, Joint 1, is pulled by the tension of  $F_1$ . The torque  $\tau_3$  acting on distal joint 3 equals to  $F_3$  times  $r$ . Interestingly, the same magnitude torques are generated both on proximal joints 2 and 1; thus, the proximal Joint 1 torque consequently becomes  $(F_1 + F_2 + F_3)r$ . Qualitatively, the tension to generate the torque for the distal joint can be added to the proximal joint by this mechanism. Consequently, a huge gravitational torque on the proximal joint can be shared by multiple tendons. Please see references [9][10] for more details.

### B. WEIGHT COMPENSATION MECHANISM

In addition to the coupled tendon-driven mechanism, we introduce a special thick tendon, called the weight compensation tendon (WCT), to achieve a higher payload with a small width. The rope strength increases in proportion to the cross-section area of the rope. In other words, the strength of the rope is proportional to the square of its radius. Therefore, compared to the equally increase in all radii of the tendons, introducing one thick tendon is quite effective in increasing the maximum payload with the limited arm width. Figure 4 shows the basic idea of this design. The red line depicts the thick tendon pulled by a large actuator. This actuator

mainly compensates for the gravity torque depending on the global posture of the arm. Smaller actuators control the blue tendons and achieve individual joint control.

The WCT tension,  $F_w$ , should be controlled depending on the arm posture. The gravity torque becomes a maximum value when the arm horizontally extends. No gravity torque occurs when the arm takes a completely vertical posture. Therefore,  $F_w$  should be optimized based on the global (overall) posture of the arm, which is explained in the section that follows. In addition, the gravity torque differs because of the joint location. The proximal joint requires a larger compensation torque, whereas the distal joint needs a smaller compensation torque. We introduce double pulleys in Fig.5 to solve this problem, where  $r_{wi}$  is the smaller radius,  $R_{wi}$  is the larger radius, and  $\tau_{wi}$  is the resultant torque. The WCT tension is reduced by adjusting the ratio of the double pulley radii  $r_{wi}/R_{wi}$ . The derivation of the optimum radii of the double pulleys was studied in [14].

### C. YAW JOINTS

For a long-reach manipulator to have a large workspace in a three dimensional (3D) space is desirable. In our previous work, we proposed the installation of the yaw axes in addition to the pitch axes in the distal segments of the arm [10]. Figure 6 illustrates the pulley arrangement demonstrating both pitch and yaw bending by a coupled tendon-driven mechanism. The yaw rotation is generated when one of the antagonistic tendons is pulled, and the other is relaxed. Meanwhile, the pitch rotation is generated when both tendons are pulled. By means of this, the actuators for the yaw joints can be utilized to generate torques around the proximal pitch axes while keeping the same yaw joint angle.

### D. JOINT CONFIGURATION AND ARRANGEMENT OF TENDONS AND PULLEYS

Figure. 7 depicts the joint configuration and arrangement of the tendons and the pulleys. The arm consists of seven segments. The proximal four segments have pitch joints, and the distal three segments have yaw and pitch joints because a 3D motion is required close to the center of the PCV. The WCT is introduced to the proximal five pitch joints to compensate for the huge gravity torques. All

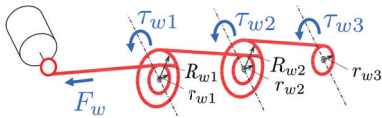


Fig. 5. Double pulleys to obtain appropriate weight compensation torques.

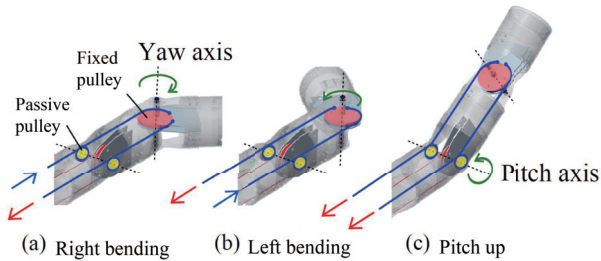


Fig. 6. Coupled tendon-driven mechanism for the yaw / pitch joints [10].

actuators are installed on the base structure to reduce the arm weight as much as possible. Moreover, this structure achieves a high radiation resistance because the arm structure contains only mechanical parts, and electrical parts, including a semiconductor, which is the weakest part against radiation, can be installed away from the center of the PCV. This mechanism can also achieve ease of waterproof design. All joints are controlled by antagonistic tendons, and all tendons are wound around the proximal transfer pulleys to generate the torques against gravity. Note that the tendon pathways in Joint 5 for tendons 11 and 12 generate a positive pitching torque, which is in the same direction to that of the gravity torque. This is because the tension of the WCT - where pulley radius is  $R_{w5}$  - generates a larger torque than the gravity torque on Joint 5. We cannot decrease the radius of  $R_{w5}$  to a value smaller than that of the joint axis. Thus, we utilized JCTs to generate a positive pitching torque to counterbalance the negative pitching torque by the WCT.

## IV. CONTROL ALGORITHM

There have been numerous studies about hyper-redundant manipulator, including kinematics and dynamics [11], inverse kinematics [12] and path planning [13] studies. However, the proposed coupled tendon-driven mechanism imposes a highly coupled interaction between each joint torque unlike previous studies [4][7]. In this paper, our primary goal was to confirm hardware feasibility of the proposed mechanical design. Therefore, we do not discuss aspects pertaining to the high-level controller, such as joint trajectory planning, redundancy problem solving, and inverse kinematics solving. The goal of this section is to achieve the joint angle  $\theta$  while reducing the maximum tension of the joint control tendons (JCTs), whereby the arm motion is quasi-static, in the absence of applications of external forces or torques.

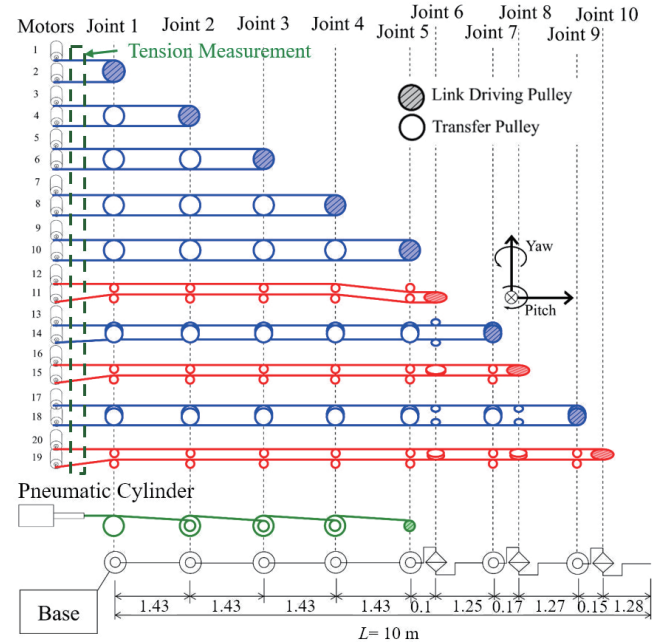


Fig. 7. Joint configuration and tendon-pulley arrangement.



Therefore, we only consider the static balance in the gravity field.

First, we discuss the formulations of the conventional coupled tendon-driven mechanism based on the previous work [9]. Second, we introduce the WCT and discuss the derivation of the appropriate tension [14].

Let us discuss the coupled tendon-driven mechanism depicted in the blue and red lines in Fig. 7. No external force and torque are applied; thus, the joint torque  $\boldsymbol{\tau} = \{\tau_i\} \in \mathbb{R}^{10 \times 1}$  is simply calculated by the arm posture, where the joint angles  $\boldsymbol{\theta} = \{\theta_i\} \in \mathbb{R}^{10 \times 1}$ , and the function  $\mathbf{g}$  determines the gravitational torque which depends on  $\boldsymbol{\theta}$ :

$$\boldsymbol{\tau} = \mathbf{g}(\boldsymbol{\theta}). \quad (1)$$

$\boldsymbol{\tau}$  is also expressed using the tension of the JCTs,  $\mathbf{F} = \{F_i\} \in \mathbb{R}^{20 \times 1}$

$$\boldsymbol{\tau} = \mathbf{R}\mathbf{F}, \quad (2)$$

where  $\mathbf{R} \in \mathbb{R}^{10 \times 20}$  is a coefficient matrix to represent the pulley radii and arrangement of the JCTs. We cannot directly solve Eq. (2) because  $\mathbf{R}$  has no inverse matrix. In particular, the bias tensions for the yaw joints drawn in the red lines in Fig. 7 can be arbitrarily set with the upper limit. We can analytically optimize the tensions using unified tendon-traction control proposed in [9].

Assuming no elongation and no slack of tendons, the position commands to the actuators to control the JCTs are uniquely determined because the relationship between the joint angle displacement  $\Delta\boldsymbol{\theta} \in \mathbb{R}^{10 \times 1}$  and the amount of tendon winding/unwinding  $\mathbf{S} \in \mathbb{R}^{10 \times 1}$  is expressed using  $\mathbf{R}^T$ :

$$\mathbf{S} = \mathbf{R}^T \Delta\boldsymbol{\theta}. \quad (3)$$

Next, we introduce the WCT that generates torques on the proximal five joints (1, 2, ..., 5) drawn in the green line in Fig. 7. The weight compensation joint torque  $\boldsymbol{\tau}_w$  and its displacement  $S_w$  are derived as follows:

$$\boldsymbol{\tau}_w = \mathbf{R}_w(F_w), \quad (4)$$

$$S_w = \mathbf{R}_w^T \Delta\boldsymbol{\theta}_w, \quad (5)$$

where  $\mathbf{R}_w \in \mathbb{R}^{5 \times 1}$  is a coefficient matrix determined by the double pulley radii and pulley arrangement, and  $\Delta\boldsymbol{\theta}_w \in \mathbb{R}^{5 \times 1}$  is the displacement of the WCT. Hence, Eq. (2) is re-written as follows:

$$\boldsymbol{\tau} = \mathbf{R}\mathbf{F} + \mathbf{R}_w(F_w). \quad (6)$$

The objective here is to optimize  $\mathbf{F}$  and  $F_w$  in real time when  $\boldsymbol{\theta}$  is given. We adjust the bias tensions for  $\mathbf{F}$  and  $F_w$  to reduce the maximum of the tension of the JCTs,  $F_{\max} = \max\{F_i\}$ . Moreover, the tendon tension must be positive at all postures because the tendon cannot generate a negative force. Therefore, we set the tendon tension as follows:

$$F_w \geq F_{w\min} \geq 0 [\text{N}] \quad (7)$$

$$F_i \geq F_{i\min} \geq 0 [\text{N}] \quad (i = 1, 2, \dots, 20) \quad (8)$$

where  $F_{w\min}$  and  $F_{i\min}$  ( $i = 1, 2, \dots, 20$ ) are the minimum tendon tensions for the WCT and the JCTs to prevent the tendon slack, respectively. Our long-reach manipulator does not generate a rapid movement; thus, we can search for  $F_w$  and  $\mathbf{F}$  using a simple algorithm to solve the non-linear problem under the conditions of Eqs. (7) and (8). We use a gradient descent method as a function  $F_{\max}$  of the tendon tension  $\{\mathbf{F}, F_w\}$ . Given the small perturbations of the bias tensions for  $\mathbf{F}$ , and  $F_w$ , we directly compute  $\mathbf{F}$  with Eqs. (1) and (2) from the distal joint to the proximal joint sequentially.  $\mathbf{F}$  is uniquely determined, and we check whether  $F_{\max}$  is decreased or not. This calculation is terminated when  $F_{\max}$  becomes sufficiently small. Although the gradient decent method cannot guarantee a global optimum and it may be captured on a local minimum, this method provides smooth tension transitions during the search process. This property is essential for our initial hardware verification because JCTs are highly coupled to each other, and discontinuous tension changes may considerably decrease control stability for each joint. The longest time expended for obtaining a solution was only 23 ms using a PC (Core i7-4910MQ, 2.9 GHz, Intel).

## V. MECHANICAL DESIGN OF THE PROTOTYPE

As shown in Fig. 1, the prototype model is divided into the arm structure and the base structure. The arm structure consists of the joint mechanism with multiple pulleys and tendons, CFRP pipes, and potentiometers for the joint angle measurement. The base structure contains actuators, reel mechanisms, actuator drivers, and tension sensors.

### A. ARM STRUCTURE DESIGN

Figure 8 shows the detailed design of the first proximal joint that contains the most numerous transfer pulleys. The link is made of the CFRP pipe with a 2 mm thickness. The aluminum alloy parts are fixed at both link ends. The pulley thickness should be minimized as much as possible to install many transfer pulleys inside the limited arm diameter, which leads to a structural outer surface deformation. We install multiple thrust needle roller bearings between two adjacent transfer pulleys to prevent this undesirable deformation. In regard to pulley radii, we maximized the pulley radii as much

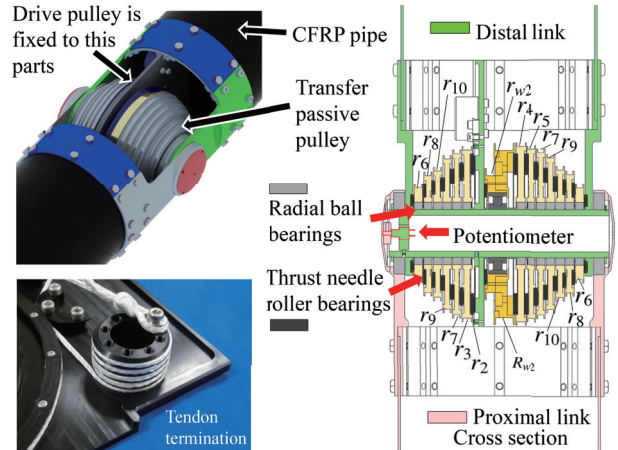


Fig. 8. Detailed mechanism of the first proximal joint.

as possible to fit the diameter of the CFRP pipe to generate maximum joint torques. We arranged the WCT pulley in the middle of the joint axis to achieve the maximum WCT pulley diameter, while the proximal JCT pulleys were located on the inner parts, and the distal pulleys were on the outer parts. These pulley radii were also adjusted depending on the mass distribution of the arm structure, which was estimated by 3D CAD model. The designed coefficient matrix  $\mathbf{R}$  and vector  $\mathbf{R}_w$  can be found in the Appendix.

A potentiometer (JC10-000-103N, NIDEC COPAL Corp.) is installed inside the joint shaft to measure the joint angle. This is the only electric part in the arm structure, which is a passive electric element that has high radiation resistance compared with an encoder using semiconductors. Therefore, this arm design can achieve a high radiation resistance. The estimated weight of the arm structure was only 49.9 kg, and the maximum diameter of the link was 194 mm, suggesting that the proposed design can be extremely lightweight and slim.

### B. BASE STRUCTURE DESIGN

Figure 9 shows the side view of the base structure and the tendon pathways. Twenty DC actuators with planetary gear heads (RE40, 1/113, Maxon) are installed to wind the JCTs. The actuator output is connected to a reel mechanism via the spur gear reducer (16/75) shown in the blue frame in

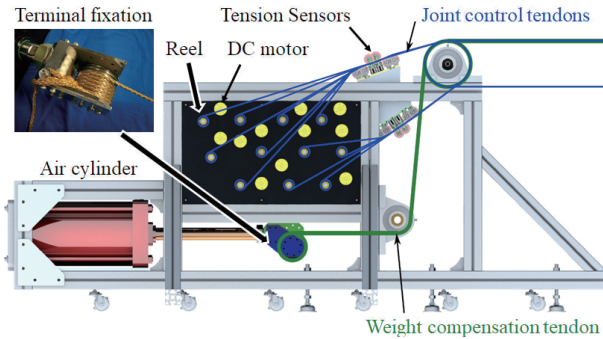


Fig. 9. Base structure: arrangement of the actuators and the tendon pathways.

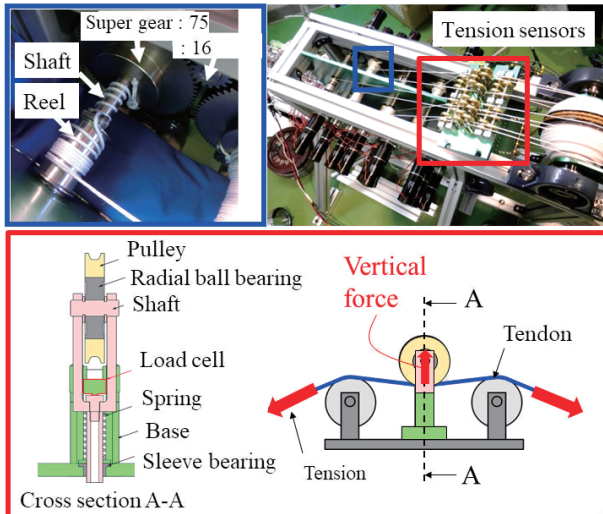


Fig. 10. Reel mechanism (blue) and tension sensor (red).

Fig. 10. A 30 mm reel diameter is selected, which achieves a maximum tension greater than 90 % of the tensile strength, based on our previous work to investigate the strength decrease caused by pulley bending [15]. The arrangement of the DC actuators was optimized to minimize the size of the base structure while keeping the JCTs pathways clear and the maintenance easy.

All the tensions of the JCTs are measured by the custom-made tension sensors shown in the red frame in Fig. 9. The tendon goes through three passive pulleys, and a load cell (MCDW-50L, TOYO-SOKKI) is installed inside the middle pulley to measure the vertical force generated by the tendon tension.

We decided to use a pneumatic cylinder (10A-2FB200B300, Taiyo), which is lightweight compared to the electric actuator, to generate a huge force to pull the WCT. This air cylinder can pull the WCT up to 30.2 kN, and the tension of the WCT is controlled by an electropneumatic regulator (EVD-3900, CKD). The estimated total weight of the base structure was approximately 250 kg.

### C. SYNTHETIC FIBER ROPE

Nowadays, synthetic fiber ropes have larger tensile strengths than metal ropes despite them being very lightweight. Moreover, synthetic fiber ropes permit us to design a compact mechanism, thanks to their high flexibility and durability against sharp bending.

We selected a 2 mm-diameter Dyneema rope (tensile strength of 4.29 kN, DB-96HSL, Hayami industry) as the JCTs because of these characteristics. We intensively investigated the basic mechanical properties of various types of synthetic fiber ropes in our previous work [15] [16] [17], and found that Dyneema had the highest durability against sharp repetitive bending.

However, fixing the Dyneema rope to the drive pulley is very difficult because of the low friction coefficient. Therefore, we developed a new terminal fixation method using a grooved pulley and a figure-eight knot hanging on a pin [18] shown in Fig. 8. It can support the tension greater than 90 % of the tensile strength.

As regards the WCT, we selected a 5.5 mm-diameter Zylon rope (tensile strength of 46.1 kN, ZB-15728, Hayami industry). Although the Zylon rope does not have a higher durability against repetitive bending, Zylon has the highest tensile strength. Moreover, the weight compensation tendon is not frequently driven compared with the JCTs. Thus, we concluded that the Zylon rope was the best for the WCT. We also introduced our new terminal fixation method shown in Fig. 9 and confirmed that it could fix the tension of 30 kN.

We are currently measuring the radiation resistance of the synthetic fiber ropes by exposing  $\gamma$ -ray. The initial result revealed no significant strength reduction up to 10 kGy for Dyneema and Zylon. We can estimate an operation time of 133 h under the highest radiation dose level of 75 Gy/h in the No. 2 reactor. We believe that the operation time is sufficient because the camera previously used in [1] could endure up to only 1 kGy.

#### D. CONTROL SYSTEM

Figure 11 shows the control system. The external control PC sends the desired joint angles and desired tensions for the JCTs to the micro controllers. The micro controllers control the DC actuators and air pressure, and measure the joint angles and the JCT tensions every 10 ms. The micro controllers return the measured joint angles, measured tensions, and PWM commands of each DC actuator to the external control PC. The operator can manually set the desired joint angles using the external PC every 100 ms.

Figure 12 shows the block diagram the JCT actuators. Two PI controllers are used to achieve the target joint angle and the target tendon tension. These two outputs are weighted with manually tuned parameters and sent to the actuators. All PWM commands to the motor drivers are monitored not to exceed the specified maximum tension of the JCTs to prevent the rope break.

#### E. ASSEMBLY

We first assembled a four-segment model, whose length was 5.72 m (Fig. 13), to verify the performance of the mechanism step by step. The proximal two segments and the second distal two segments were connected, and the arm became 6 DoF (pitch: 4; yaw: 2), which was the same joint arrangement of Mini3DCT-Arm [10]. The proximal three pitch joints were supported by the WCT. The detailed joint photos show that the first joint (Joint 1) had many transfer pulleys, whereas the last joint (Joint 8) had a single

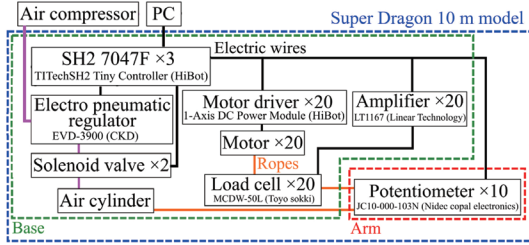


Fig. 11. System configuration of Super Dragon.

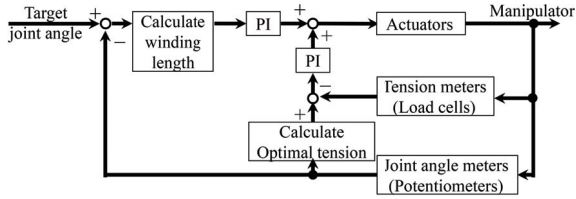


Fig. 12. Control block diagram for each JCT.

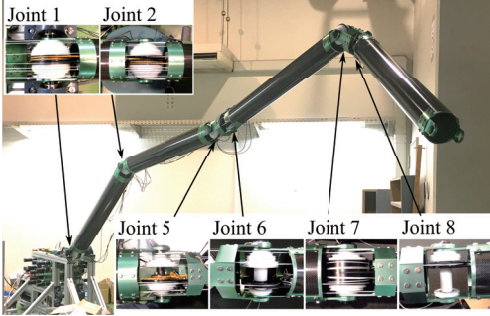


Fig. 13. Super Dragon 5.7 meter model.

tendon. We constructed a 10 m model after verifying the basic function using the 5.7 m model.

#### VI. EXPERIMENT

An end-point control experiment supposing an inspection task was performed to verify the control system using the 5.7 m model. The target task of this experiment was to capture the four predefined targets using an onboard camera attached at the arm end. Because the most important task for the initial investigation in the PCV is to capture internal images by remotely controlling the direction of a camera. We considered that the positioning experiment was a success when the distance between the end-point and the target marker was less than 0.35 m. (This evaluation criterion was considered sufficient accuracy for the initial investigation task in Fukushima by a company in charge of decommissioning.) In this case, the size of the acquired image of the target marker was approximately  $320 \times 320$  pixels. We also measured the accuracy of the joint angle control and tension control to elucidate the performance of the prototype according to this experiment. With regard to the target joint angle, the operator manually controlled each desired joint angle using graphical user interface on control PC. The operator modulated each desired joint angle by directly seeing the arm posture as well as captured images of onboard camera.

Figures 14 and 15 show snapshots of the experiments with the onboard camera images and the end-point trajectories, respectively. Figures 16 and 17 depict the time courses of

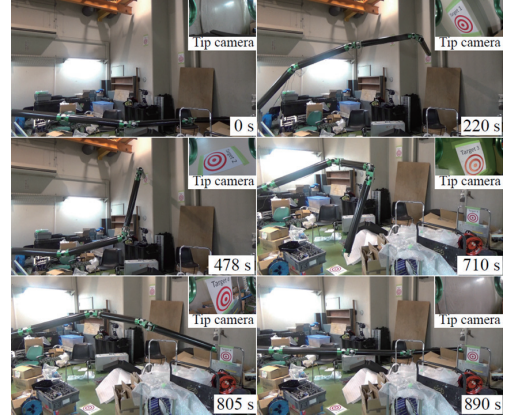


Fig. 14. End-point control experiment to capture the target markers.

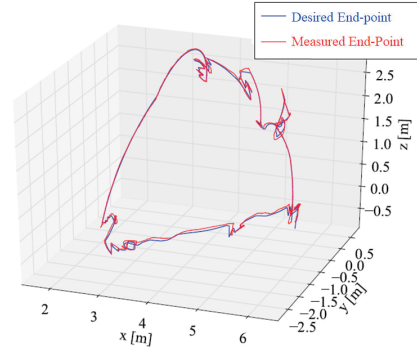


Fig. 15. Trajectories of the end point in the world coordinate. Note that the measured end-point trajectory is derived using forward kinematics with the measured joint angles.



the joint angles and the tendon tensions, respectively. We succeeded in capturing all the four target markers. The maximum distance between the end-point and target marker was 0.31 m. The averaged joint angle error was 0.8 deg, while the maximum error was 7.7 deg mainly because of the slow response of the joint control system. The joint angle errors resulted in the averaged end-point position error of 66 mm, which was 1.1% of the arm length. This result suggested sufficient accuracy for an inspection task. As regards the tendon tensions, the average tension error of the joint control tendons was 64.7 N. All tensions of the JCTs and the WCT were successfully kept smaller than approximately 1.7 kN and 8.5 kN, which were 40% and 18% of the breaking tensions, respectively.

Interestingly, the yaw joint control tendons  $F_{11,12,15,16}$  in Fig.17, which did not require a large joint torque, also generated substantial bias tensions. For example, the magnitudes of  $F_{15,16}$  were larger than 1 kN during the interval of 300 - 800 s. These bias tensions generated a pitching torque which was approximately equal to 50 Nm in Joint 1 and 2 in the lifting direction because the pulley radii in these were approximately equal to 50 mm. This result indicated that the yaw control tendons contributed to supporting the gravity torques acting on the pitch joints, suggesting the effectiveness of the proposed tendon-driven mechanism.

Next, we performed the experiment using the 5.7 m model with 10 kg additional mass at the arm tip to prove the large payload capability. We selected the horizontally extended

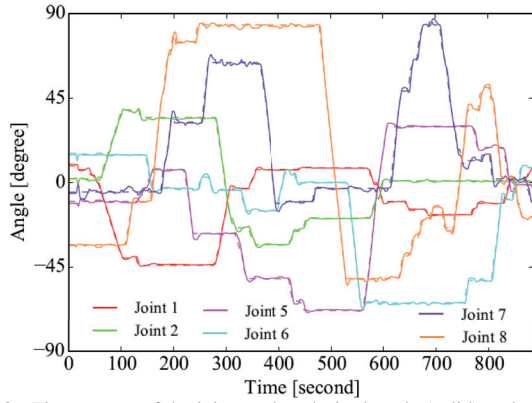


Fig. 16. Time course of the joint angles: desired angle (solid) and measured angle (dashed).

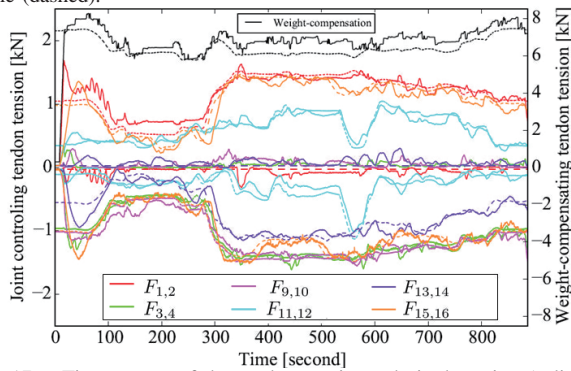


Fig. 17. Time course of the tendon tensions: desired tension (solid) and measured tension (dashed).  $F_{2i-1}$  and  $F_{2i}$  ( $i = 1, 2, 5, 6, 7, 8$ ) are antagonistic pair tendons drawn with the same color. Note that all tensions of  $F_{2i}$  have a negative sign.

posture to maximize the gravity torque acting on the arm. As shown in Fig.18, we succeeded in keeping a horizontal posture with the 10 kg payload. The maximum tensions of the JCTs and the WCT were approximately 1.5 kN and 11.6 kN, which were still 35% and 25% of the breaking tensions, respectively.

Finally, we constructed a 10 m model and confirmed its feasibility by the hardware experiments. The total system was assembled in the experiment room and successfully moved outdoors through double doors of W 3.0 m  $\times$  H 2.5 m by 10 people. We used water tanks (approx. 250 kg in total) for stabilization to prevent tumbling. This outdoor experiment suggested ease of deployment compared to the previous works [3] [4] [7].

In our preliminary experiment, some transfer pulleys were broken because we manufactured them with engineering plastic (POM), which was lightweight. Moreover, some JCTs were also broken because of the large latency in the tension control feedback loop. Therefore, we improved the design of the broken pulley with aluminum alloy (A2017) and selected heat-set Dyneema with stronger fiber yarns (tensile strength 7.17 kN, single braid Dyneema SK99 [HPS+PU] without a cover, NA20020SOC00\001.000, Armare).

Eventually, we verified that the 10 m-long arm was successfully lifted up, and the horizontal posture was kept, as shown in Fig. 19. We also performed a target tracking experiment using the distal three segments similar to the 5.7 m model and confirmed the sufficient control performance to locate the end-point of the arm.

## VII. CONCLUSION

This study discussed a 10 m-long articulated manipulator for the decommissioning task in the Fukushima Daiichi NPPs. We introduced a coupled tendon-driven mechanism and a weight compensation mechanism using synthetic fiber ropes to design a lightweight, compact, and high-payload manipulator. We developed a 5.7 m- and 10 m-long prototype model and confirmed its feasibility through basic motion experiments.

In our future works, we plan to evaluate the end-point positioning accuracy with a 10 m-long model using a 3D laser scanner. The high-payload experiment with the 10

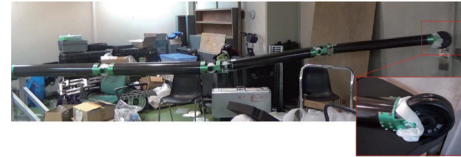


Fig. 18. 5.7 m model lifting 10 kg weight.



Fig. 19. Experiment on keeping the horizontally extended posture using the 10 m model.



## APPENDIX

The coefficient matrix  $\mathbf{R}$  and the vector  $\mathbf{R}_w$  represent the pulley radii and arrangement of the JCTs, and double pulley radii and pulley arrangement of the WCT, respectively.

$$\mathbf{R} = \begin{bmatrix} -82.5 & 0 & 0 & 0 & 0 & 0 & 0 & 0 & 0 & 0 \\ 82.5 & 0 & 0 & 0 & 0 & 0 & 0 & 0 & 0 & 0 \\ -75.5 & -75.5 & 0 & 0 & 0 & 0 & 0 & 0 & 0 & 0 \\ 75.5 & 75.5 & 0 & 0 & 0 & 0 & 0 & 0 & 0 & 0 \\ -72.5 & -70.5 & -70.5 & 0 & 0 & 0 & 0 & 0 & 0 & 0 \\ 72.5 & 70.5 & 70.5 & 0 & 0 & 0 & 0 & 0 & 0 & 0 \\ -73 & -73.5 & -73.5 & -73.5 & 0 & 0 & 0 & 0 & 0 & 0 \\ 73 & 73.5 & 73.5 & 73.5 & 0 & 0 & 0 & 0 & 0 & 0 \\ -72.5 & -70.5 & -71 & -66 & -65 & 0 & 0 & 0 & 0 & 0 \\ 72.5 & 70.5 & 71 & 66 & 65 & 0 & 0 & 0 & 0 & 0 \\ -39.5 & -38 & -37.5 & -35 & 23 & -57 & 0 & 0 & 0 & 0 \\ -39.5 & -38 & -37.5 & -35 & 25 & 57 & 0 & 0 & 0 & 0 \\ -69.5 & -67.5 & -67.5 & -64.5 & -60.5 & -25.5 & -57.5 & 0 & 0 & 0 \\ 69.5 & 67.5 & 67.5 & 64.5 & 60.5 & 25.5 & 57.5 & 0 & 0 & 0 \\ -50.5 & -49 & -49 & -47 & -30.5 & -49 & -27.5 & -46 & 0 & 0 \\ -50.5 & -49 & -49 & -47 & -23 & 49 & -20 & 46 & 0 & 0 \\ -64.5 & -63 & -63 & -60 & -53 & 33 & -50 & 30 & -47 & 0 \\ 64.5 & 63 & 63 & 60 & 53 & -33 & 50 & -30 & 47 & 0 \\ -54.5 & -53 & -53 & -54.5 & -45.5 & -41 & -42.5 & -38 & -39.5 & -35 \\ -54.5 & -53 & -53 & -54.5 & -38 & 41 & -35 & 38 & -32 & 35 \end{bmatrix}^T \quad [\text{mm}]$$

$$\mathbf{R}_w = [-74.0 \quad -46.9 \quad -25.5 \quad -12.0 \quad -6.09 \quad 0.00 \quad 0.00 \quad 0.00 \quad 0.00 \quad 0.00] \quad [\text{mm}]$$

m-long model was an important experiment to prove the effectiveness of our mechanical design. In regard to control algorithm, we need to investigate a high level controller such as inverse kinematics and path planning.

## ACKNOWLEDGMENT

The authors want to thank Prof. Koichi Suzumori and Assist. Prof. Hiroyuki Nabae for their invaluable discussions. We would like to express our gratitude to Mr. Youki Wakabayashi and Mr. Takuma Yabuta who helped us a lot in improving the mechanical design for the 10 m model. We received generous support from the students and staffs of the Suzumori-Endo laboratory when we performed the experiments. This study was based on the results obtained from a project commissioned by the New Energy and Industrial Technology Development Organization (NEDO).

References are important to the reader; therefore, each citation must be complete and correct. If at all possible, references should be commonly available publications.

## REFERENCES

- [1] IRID R&D Topics DEVELOPMENT OF ROBOT "PMORPH" FOR INVESTIGATION INSIDE UNIT 1 PRIMARY CONTAINMENT VESSEL (PCV). 2017. [Online]. Available: <http://irid.or.jp/en/topics/>
- [2] IRID R&D Topics INVESTIGATION INSIDE PRIMARY CONTAINMENT VESSEL (PCV). 2017. [Online]. Available: <http://irid.or.jp/en/topics/>
- [3] IRID R&D Topics DEVELOPMENT OF "ROBOT ARM / ACCESS RAIL". 2017. [Online]. Available: <http://irid.or.jp/en/topics/>
- [4] B. Haist, S. Mills, and A. Loving, "Remote handling preparations of JED EP2 shutdown", *Fusio. Engin. Desig.*, Vol. 84, 2009, pp. 875-879.
- [5] L. Snoj et al., "Calculations to support JET neutron yield calibration: Modelling of the JET remote handling system", *Nuclea. Engin. Desig.*, Vol. 261, 2013, pp.244-250.
- [6] Octant 1 boom extension. 2009. [Online]. Available: <http://www.ccf.ac.uk/assets/Documents/Services/CS-RHO1BE.pdf>
- [7] Y.Perrot et al., "Long-reach Articulated Robots for Inspection and Mini-Invasive Interventions in Hazardous Environments: Recent Robotics Research, Qualification Testing, and Tool Developments, *Journ. Field. Robot.*, Vol. 22, No.1, 2012, pp.175-185.
- [8] M. Takeichi, K. Suzumori, G. Endo, and H. Nabae, "Development of a 20-m-long Giacometti Arm with Balloon Body ased on Kinematic Model with Air Resistance, in *Proc. IEEE Int. Conf. Intel. Robot. Syste.*, Vancouver, Canada, 2017, pp.2710-2716.
- [9] S. Ma, S. Hirose, and H. Yoshinada, "Design and Experiments for a Coupled Tendon-Driven Multijoint Manipulator.", *IEEE Cont. Sys. Magaz.*, Vol. 13, Issue. 1, 1993, pp. 30-36.
- [10] A. Horigome, H. Yamada, G. Endo, S. Sen, S. Hirose, and E.F. Fukushima, "Development of a Coupled Tendon-Driven 3D Multijoint Manipulator.", in *Proc. IEEE Int. Conf. Robot. Autom.*, Hong Kong, China, 2014, pp.5915-5920.
- [11] W. Xu, T. Liu, and Y. Li, "Kinematics, Dynamics, and Control of a Cable-Driven Hyper-Redundant Manipulator.", *IEEE/ASME Tran. on Mecha.* Vol. 23, Issue. 4, 2018, pp. 1693-1704.
- [12] S. Yahya et al., "A Geometrical Inverse Kinematics Method for Hyper-Redundant Manipulators.", in *Proc. IEEE Int. Conf. Symp. Cont. Autom. Robot. Vision*, Hanoi, Vietnam, 2008, pp.1954-1958.
- [13] L. Blaha, and M. Svejda, "Path planning of hyper-redundant manipulator in developed view.", in *Proc. 19th Int. Carpa. Cont. Conf.*, Krakow-Wieliczka, Poland, 2018, pp. 295-300.
- [14] A. Horigome, G. Endo, K. Suzumori, and H. Nabae, "Design of a Weight-compensated and Coupled Tendon-driven Articulated Long-reach Manipulator.", in *Proc. IEEE/SICE Int. Symp. Sys. Integr.*, Sapporo, Japan, 2016, pp.598-603.
- [15] A. Horigome and G. Endo, "Basic study for drive mechanism with synthetic fiber rope -investigation of strength reduction by bending and terminal fixation method.", *Advan. Robot.*, Vol. 30, Issue 3, 2016, pp. 206-217.
- [16] A. Horigome, and G. Endo, "Investigation of Repetitive Bending Durability of Synthetic Fiber Ropes", *IEEE Robot. Autom. Letter*, Vol. 3, No. 3, 2018, pp.1779-1789.
- [17] A. Takata, G. Endo, K. Suzumori, H. Nabae, Y. Mizutani, and Y. Suzuki, "Modeling of Synthetic Fiber Ropes and Frequency Response of Long-Distance Cable-Pulley System", *IEEE Robot. Autom. Letter*, Vol. 3, No. 3, 2018, pp.1743-1750.
- [18] A. Horigome, G. Endo, A. Takata, and Y. Wakabayashi, "Development of New Terminal Fixation Method for Synthetic Fiber Rope", *IEEE Robot. Autom. Letter*, 2018, DOI: 10.1109/LRA.2018.2851033